Manifestation of incoherent-coherent crossover and non-Stoner magnetism in the electronic structure of Fe₃GeTe₂

Deepali Sharma, Asif Ali, Neeraj Bhatt, Rajeswari Roy Chowdhury, Chandan Patra,
Ravi Prakash Singh, and Ravi Shankar Singh*

Department of Physics, Indian Institute of Science Education and Research Bhopal, Bhopal Bypass Road, Bhauri, Bhopal 462066, India

Two-dimensional (2D) van der Waals ferromagnets have potential applications as next-generation spintronic devices and provide a platform to explore the fundamental physics behind 2D magnetism. The dual nature (localized and itinerant) of electrons adds further complexity to the understanding of correlated magnetic materials. Here, we present the temperature evolution of electronic structure in the 2D van der Waals ferromagnet Fe₃GeTe₂ using photoemission spectroscopy in conjunction with density functional theory (DFT) plus dynamical mean field theory (DMFT). With the appearance of a quasiparticle peak and its evolution in the vicinity of the Fermi energy, we unveil empirical evidence of an incoherent-coherent crossover at around 125 K. DFT+DMFT results show that the quasiparticle lifetime surpasses thermal energy for temperature below 150 K, confirming incoherent-coherent crossover in the system. The lack of appreciable change in the Fe 2p core level, overall valence band spectra across the magnetic transition, and temperature-dependent ferromagnetic DFT+DMFT results provide substantial evidence for non-Stoner magnetism in Fe₃GeTe₂. We elucidate the temperature-dependent intimate relation between magnetism and electronic structure in Fe₃GeTe₂. A Sommerfeld coefficient of ∼104 mJ mol⁻¹ K⁻² obtained in the low-temperature limit from DFT+DMFT calculations resolves the long-standing issue of a large Sommerfeld coefficient (∼110 mJ mol⁻¹ K⁻²) obtained from specific heat measurements.

I. INTRODUCTION

Magnetism in two-dimensional (2D) van der Waals (vdW) materials have been the subject of great interest because of their ordered magnetic phases down to the monolayer limit [1–3]. The magnetic and electronic ground states of these 2D materials can be manipulated by external stimuli such as strain, gating, proximity effects, etc., and the easy exfoliation allows the fabrication of novel devices down to the 2D limit [2,3]. In this class of ferromagnets, Cr₂Ge₂Te₆, CrSiTe₃, CrI₃, etc., have been widely studied due to the rich interplay between long-range magnetic ordering, intersite exchange J, and intrasite Coulomb U interactions in deciding the electronic structure [4–6].

Fe₃GeTe₂, a 2D vdW ferromagnet, has attracted enormous attention due to the remarkably high Curie temperature ($T_C \sim$ 220 K), large uniaxial magnetocrystalline anisotropy persisting down to the monolayer limit, magnetic skyrmions, the anomalous Hall effect, etc. [7–10]. Density functional theory (DFT) reveals the itinerant ferromagnetism fulfilling the Stoner criteria [11,12], which is supported by photoemission spectroscopy (PES) exhibiting continuous spectral weight transfer within Fe 3d states (the signature of exchange splitting) in the ferromagnetic phase [13]. However, in complete contrast, another report using angle-resolved PES (ARPES) revealed an insignificant change in the band dispersion with increasing temperature up to T_C [14].

In general, the nature of ferromagnetism is understood from (1) the Stoner model in the case of itinerant bands, where the temperature-dependent exchange splitting of dispersive spin bands drives the long-range magnetic ordering, which eventually vanishes upon reaching T_C, or (2) the spin mixing model in the case of localized bands, where the exchange splitting exists even above T_C and the thermal fluctuation of the local moment reduces the magnetization [15–17]. However, many magnetic materials fall in the intermediate regime of itinerant-local moments, such as cuprates and iron pnictides, due to the rich interplay of electronic states and magnetic correlations [15–21]. Although Fe₃GeTe₂ is a d-electron system, coexisting localized and itinerant electrons drive Fe₃GeTe₂ to a heavy-fermionic state at low temperature [13,22,23]. The electronic transport and magnetic measurements indicate the signature of incoherent-coherent crossover far below T_C, along with the Fano-resonance feature in the scanning tunneling spectra concluding the Kondo scenario [13,23,24]. The large effective mass (∼13.3$m_{\rm DFT}$) from the Sommerfeld coefficient ($\gamma =$ 110 mJ mol⁻¹ K⁻²) obtained from specific heat measurements is not adequately reproduced by ARPES and dynamical mean field theory (DMFT) calculations across the literature [13,14,25,26]. Understanding the nature of ferromagnetism (Stoner versus non-Stoner), the incoherent-coherent crossover, and large effective mass leading to heavy-fermionic behavior warrants a comprehensive study of the electronic structure and its relation to magnetism in both the high- and low-temperature limits.

Here, we investigate the electronic structure of Fe₃GeTe₂ using photoemission spectroscopy and theoretical

calculations within the DFT+DMFT framework. The Fe $2p$ core level spectra and valence band spectra remain very similar across T_C, except for the states close to the Fermi level E_F. High-resolution spectra unveil the emergence of a quasiparticle peak in the close vicinity of E_F in the magnetically ordered phase. The overall valence band spectra and evolution of quasiparticle peak and the manifestation of the incoherent-coherent crossover ($\sim$125 K) in the experimental spectra are very well captured within temperature-dependent ferromagnetic DFT+DMFT calculations. These results further reveal spin-differentiated behavior in Fe$_3$GeTe$_2$, where spin-up states are majorly responsible for the incoherent-coherent crossover with decreasing temperature, whereas spin-down states are already in the coherent regime. Interestingly, finite spin splitting and the ordered moment persist even at temperatures larger than $4T_C$, implying non-Stoner magnetism in Fe$_3$GeTe$_2$. Additionally, the large Sommerfeld coefficient obtained in the low-temperature limit from DFT+DMFT calculations is commensurate with results obtained from specific heat measurements, resolving prior inconsistencies.

II. METHODOLOGY

High-quality single crystals of Fe$_3$GeTe$_2$ were prepared using the chemical vapor transport method with I$_2$ as the transport agent [9,10]. Direction-dependent magnetic measurements revealed the average Curie temperature T_C to be 206 ± 4 K [9,10]. Room temperature lattice parameters were found to be $a = b = 3.99$ Å and $c = 16.33$ Å, in good agreement with a previous report [27]. In the photoemission spectroscopic measurements, the Fermi level E_F positions and energy resolutions for various radiations were obtained by measuring the Fermi edge of a clean polycrystalline silver sample at 30 K. Total energy resolutions were set to 300, 12, and 5 meV for Al $K\alpha$ ($h\nu = 1486.6$ eV), He II ($h\nu = 40.8$ eV), and He I ($h\nu = 21.2$ eV) radiations (energy), respectively. Multiple single crystals of Fe$_3$GeTe$_2$ were cleaved *in situ* at base pressure better than 4×10^{-11} mbar to ascertain the cleanliness of the sample surface and reproducibility of the data (see the Supplemental Material (SM) [28] for a survey scan and low-energy electron diffraction).

Electronic structure calculations were performed using experimental lattice parameters with 2 f.u. per unit cell. The full-potential linearized augmented plane wave method as implemented in WIEN2K [29] was used for the DFT calculations. The generalized gradient approximation of Perdew, Burke, and Ernzerhof [30] was employed for the exchange correlation functional. An $18\times18\times3$ k mesh within the first Brillouin zone was used for the self-consistent calculations. The energy and charge convergence criteria were set to 10^{-4} eV and 10^{-4} electronic charge/f.u., respectively. The EDMFT code [31] was used for the charge self-consistent DFT+DMFT calculations, with two impurity problems for Fe I and Fe II, and all five Fe $3d$ orbitals (forming three nondegenerate groups, d_{z^2}, $d_{x^2-y^2}/d_{xy}$, and d_{xz}/d_{yz}) were considered in correlated subspace. The continuous-time quantum Monte Carlo impurity solver [32] was used with the double-counting correction being *exact* [33]. The Hubbard $U = 5.0$ eV, and Hund's coupling $J = 0.9$ eV was selected for both Fe I and Fe II, in

accordance with an earlier report [26]. Analytical continuation was performed using the maximum entropy method [31] to calculate self-energy on the real axis.

III. RESULTS AND DISCUSSION

The crystal structure and Brillouin zone of Fe$_3$GeTe$_2$ are shown in Fig. 1(a). Each vdW bonded layer comprises a Fe$_3$Ge slab sandwiched between Te layers. Two crystallographically different Fe sites are shown by pink (Fe I) and gold (Fe II) spheres [9,11,23]. The high quality of the sample and clean surface obtained by *in situ* cleaving are ascertained by the sharpness of peaks and the absence of any oxide-related features in the core level spectra, as shown in Fig. 1(b) (also see Note 1 in the SM [28] for further details). All the core level spectra remain very similar to their elemental counterparts [35]. No appreciable change was observed for any of the core levels when going from 300 to 30 K. Notably, the width of Fe $2p$ core level spectra in Fe$_3$GeTe$_2$ is comparable to that of ferromagnetic iron (shown by the blue lines), while it has been found to be much smaller ($\sim$0.6 eV) in nonmagnetic systems [34,36]. The full width at half maximum (FWHM) of the asymmetric Fe $2p_{3/2}$ peak was estimated (after subtracting a Shirley-type integral background), where the FWHM was found to be $\sim$1.2 and $\sim$1.4 eV for Fe$_3$GeTe$_2$ and Fe metal, respectively. The larger width arises due to finite exchange splitting, leading to the observed dichroism in the core level spectra in the case of magnetic systems [34,37,38]. The lack of change in Fe $2p$ core level spectra in Fe$_3$GeTe$_2$ suggests that the exchange splitting does not change appreciably across T_C, indicating that the non-Stoner behavior may be applicable here. The valence band in Fe$_3$GeTe$_2$ is formed by the hybridization of mainly Fe $3d$, Ge $4p$, and Te $5p$ states and is shown in Fig. 1(c), collected using Al $K\alpha$ and He II radiations across the magnetic phase transition. Al $K\alpha$ spectra at 300 K exhibit three discernible features, labeled A, B, and C, which are found at around 6 eV, at around 3 eV, and as a broad feature below 2 eV binding energy (BE), respectively. The relative intensity enhancement of feature C with respect to features A and B while going from Al $K\alpha$ spectra to He II spectra can be understood by considering the larger photoionization cross section of Fe $3d$ states compared to that of Te $5p$ and Ge $4p$ states at lower photon energies [39], confirming the dominant contribution of Fe $3d$ states in feature C. Also, the broad feature C in Al $K\alpha$ spectra is further resolved in the He II spectra, presumably due to better energy resolution, exhibiting a peak near E_F and a shoulder structure at 1 eV BE. Surprisingly, the overall valence band spectra do not show appreciable change across the magnetic phase transition either, which is in sharp contrast to the prototypical itinerant ferromagnet SrRuO$_3$ [40,41], except for the states in the close vicinity of E_F, as shown in the inset of Fig. 1(c), where the signature of a quasiparticle peak (marked by the down arrow) at 30 K is evident (this will be further discussed in relation to the high-resolution spectra).

To understand the subtle changes in the electronic structure across the magnetic phase transition, we discuss the results of the DFT calculations. Similar to experimental observations, calculated densities of states (DOSs) in the nonmagnetic (NM) phase reveal predominant Fe $3d$ states between ± 2 eV
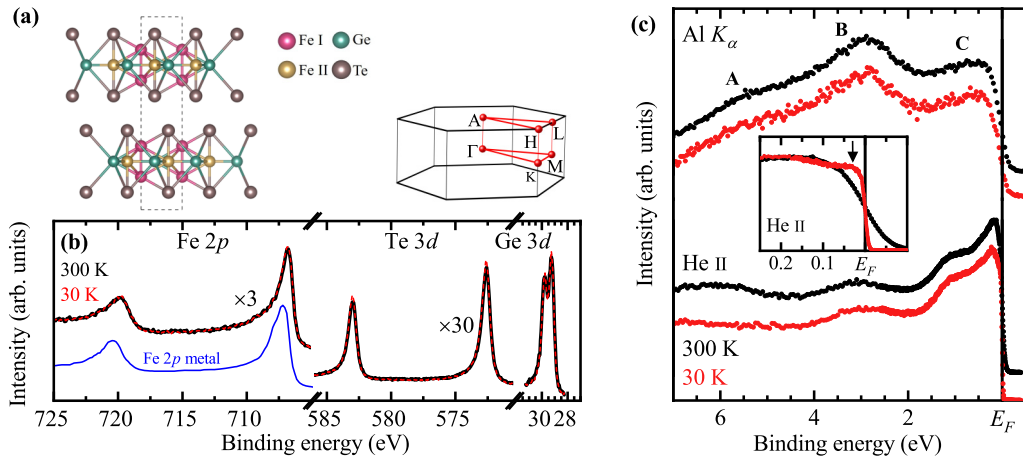
FIG. 1. (a) Crystal structure and Brillouin zone of Fe_3GeTe_2. The dashed line in the structure shows the unit cell comprising 2 f.u. (b) Core level photoemission spectra of Fe $2p$, Te $3d$, and Ge $3d$ collected at 300 K (black) and 30 K (red) using Al $K\alpha$ (intensities are normalized to that of the survey scan, Fig. S1 of the SM [28]). The spectra shown by the blue line represent the $2p$ core level of metal Fe in the ferromagnetic regime, reproduced from [34]. (c) Valence band photoemission spectra collected using Al $K\alpha$ and He II radiation at 300 K (black) and 30 K (red). The inset shows He II spectra in the vicinity of E_F.

BE [shown in Fig. 2(a)], with large states at E_F indicating metallic character. The states corresponding to Ge $4p$ and Te $5p$ primarily appear at higher BE (Fig. S3 [28]) of the SM. As expected, the total energy per unit cell decreases by 130 meV in the ferromagnetic (FM) phase, and the resulting spin-polarized DOSs are shown in Fig. 2(b). The large redistribution of exchange split spin-polarized states in the FM phase compared to the NM phase, with substan-

tial Fe $3d$ states appearing even beyond 2 eV BE, and the much reduced DOS(E_F) are in sharp contrast to the experimental observations. The obtained average magnetic moment of about $2.2\mu_B$/Fe is also an overestimation of the value ($1.6\mu_B$/Fe) obtained from the magnetic measurements [9]. Even the inclusion of Hubbard's U in DFT+U does not reproduce the experimental results (see Figs. S4 and S5 of the SM [28]). These observations are consistent with earlier
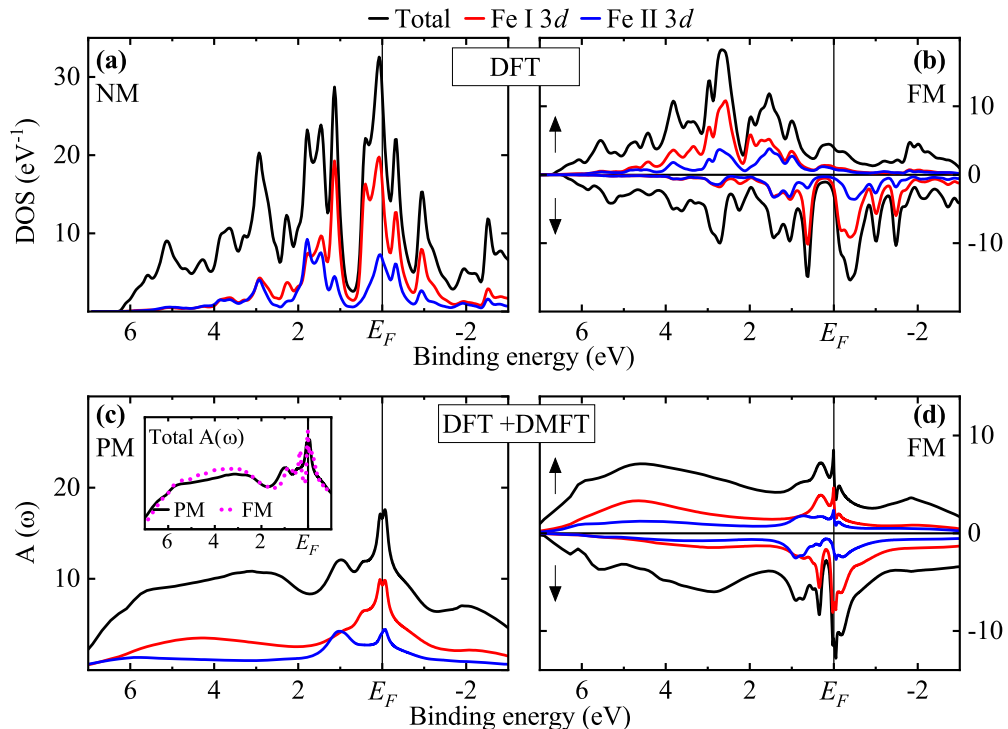

FIG. 2. Total DOS and partial DOSs of Fe I and Fe II for Fe_3GeTe_2 using (a) NM and (b) FM DFT. Total and partial spectral functions using DFT+DMFT in the (c) PM ($T = 300$ K) and (d) FM ($T = 50$ K) phases. The inset in (c) shows a comparison of total spectral functions obtained in the PM and FM DFT+DMFT phases.
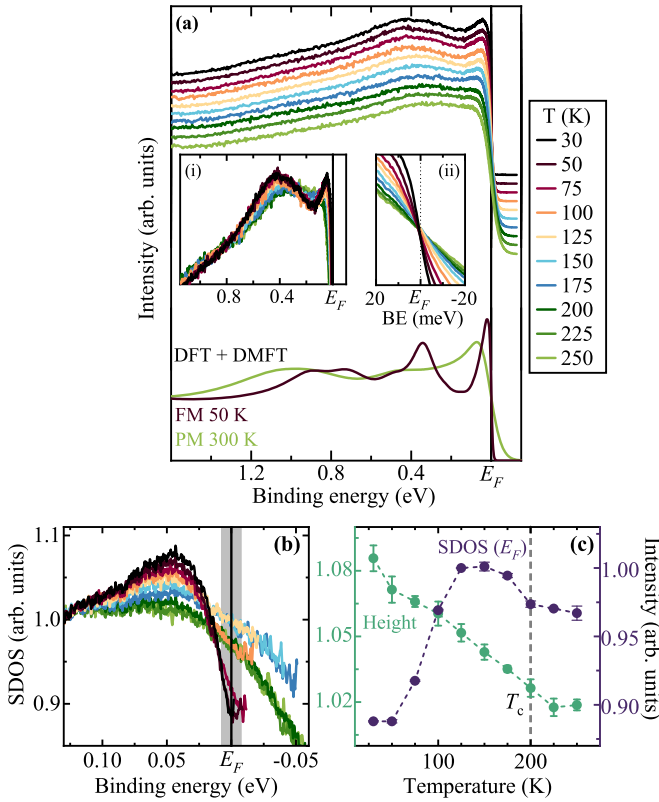
FIG. 3. (a) Temperature-dependent high-resolution valence band spectra collected using He I. The bottom plot shows the occupied part of the DFT+DMFT spectral function for the PM (300 K) and FM (50 K) phases. Inset (i): T-dependent spectral weight redistribution. Inset (ii): T evolution of the spectra in the close vicinity of E_F. T-dependent (b) SDOS in the vicinity of E_F and (c) quasiparticle peak height (green) and SDOS(E_F) (purple) obtained from (b). The shaded region in (b) represents the $\pm 3 k_B T$ range at 30 K.

studies concluding that the DFT and DFT+U fail to achieve agreement with the experimental lattice parameters, magnetic moment, and valence band spectra in the magnetically ordered phase [25,42].

Having an admixture of localized and itinerant d electrons, Fe_3GeTe_2 has been understood as a correlated electron system with a significant role played by Hund's J [43]. DFT+DMFT has been quite successful in accurately describing such systems with various magnetic transitions [44,45] since it captures the fluctuating moment in the paramagnetic (PM) phase, along with the temperature-dependent moment in the magnetically ordered phase [45–47]. In Fig. 2(c), we show the PM DFT+DMFT results for $T = 300$ K ($\beta = 38.68\ \mathrm{eV}^{-1}$), where renormalized Fe 3d bands appear between ± 1.5 eV BE. The total spectral function exhibiting a peak around E_F along with a hump at 1 eV BE is in excellent agreement with the He II spectra at 300 K. The local spin moment was found to be 1.72μ_B/Fe in PM DFT+DMFT, calculated using $\sum_i 2P_i|S_i^z|$ (where P_i and $|S_i^z|$ represent the probability and absolute spin moment, respectively). The FM DFT+DMFT result for $T = 50$ K ($\beta = 232\ \mathrm{eV}^{-1}$) shown in Fig. 2(d) exhibits a quasiparticle peak at E_F in the exchange split spin-polarized spectral functions corresponding to both the Fe sites. The total spectral function remains largely unchanged

while going from the PM to FM phase, as shown in the inset of Fig. 2(c). Further, the magnetic moment of 1.51μ_B/Fe in the FM phase is in close agreement with the experimental saturation moment [9] and closely approaches the local spin moment obtained in the PM phase. Thus, the DFT+DMFT framework successfully determines the electronic structure of Fe_3GeTe_2 in both the PM and FM phases. For further understanding of the evolution of electronic states with temperature, we show the temperature-dependent high-resolution valence band spectra collected using He I radiation in the top panel of Fig. 3(a). All the spectra are normalized by the total integrated intensity below 1.5 eV BE and have been stacked vertically for clarity. The 250 K spectra exhibit a humplike structure at ~ 1 eV BE and a broader feature below 0.5 eV BE, similar to high-temperature He II spectra [Fig. 1(c)]. With decreasing temperature, the spectral weight redistribution is evident, leading to the appearance of a sharper quasiparticle peak below 50 meV, as shown in the inset (i) of Fig. 3(a), while the broad feature at 0.4 eV BE remains very similar (within ± 0.05 eV). It should be noted here that the energy distribution curves at various k points from low-temperature ARPES are very similar to the angle-integrated spectra shown here (see Appendix A). The bottom plot shows the DFT+DMFT spectral function $A(\omega)$ obtained in the PM ($T = 300$ K) and FM ($T = 50$ K) phases multiplied by the Fermi-Dirac (FD) function to mimic the occupied states across T_C, exhibiting remarkable resemblance of the spectral evolution with the experimental spectra with respect to the overall width and energy positions of the features. To visualize the change in the electronic states in the close vicinity of E_F, we normalize the spectral intensity at 150 meV, and a closer look reveals that the temperature evolution is similar to the FD function with a small decrease in the intensity at E_F for low-temperature spectra, as shown in inset (ii). We further show the spectral DOS (SDOS) in Fig. 3(b) obtained by dividing the photoemission intensity by the resolution broadened FD function at respective temperatures [48]. The evident emergence of a quasiparticle peak at ~ 40 meV BE upon entering the FM phase is shown by the monotonous increase in its height and is plotted in Fig. 3(c) (green symbols). Interestingly, SDOS(E_F) exhibits complex and unusual evolution with temperature, as shown in Fig. 3(c) (purple symbols). SDOS(E_F) remains very similar in the PM phase, while it increases upon entering the magnetic phase and achieves a maximum at ~ 125 K, below which it decreases down to 50 K and saturates at lower temperature (also observed in the SDOS obtained by symmetrizing the spectra [49]; see Fig. S2 in the SM [28]). A change in slope in the resistivity of Fe_3GeTe_2 near a characteristic temperature ($T^* \sim 110$ K) [13,23] has been associated with an incoherent to coherent crossover similar to that in f-electron-based heavy-fermionic systems [50–52]. Below T^*, the concept of quasiparticles becomes meaningful because the quasiparticle scattering rate Γ (inverse of the lifetime) is smaller than the thermal energy $k_B T$ and sharper quasiparticle features can be observed [53]. The SDOS obtained from the high-resolution spectra [shown in Fig. 3(b)] reveals a decrease in the width of the quasiparticle peak below 125 K, also manifested by the sharp decrease in SDOS(E_F), as shown in Fig. 3(c).

We additionally showcase and meticulously explore these phenomenon using temperature-dependent FM DFT+DMFT
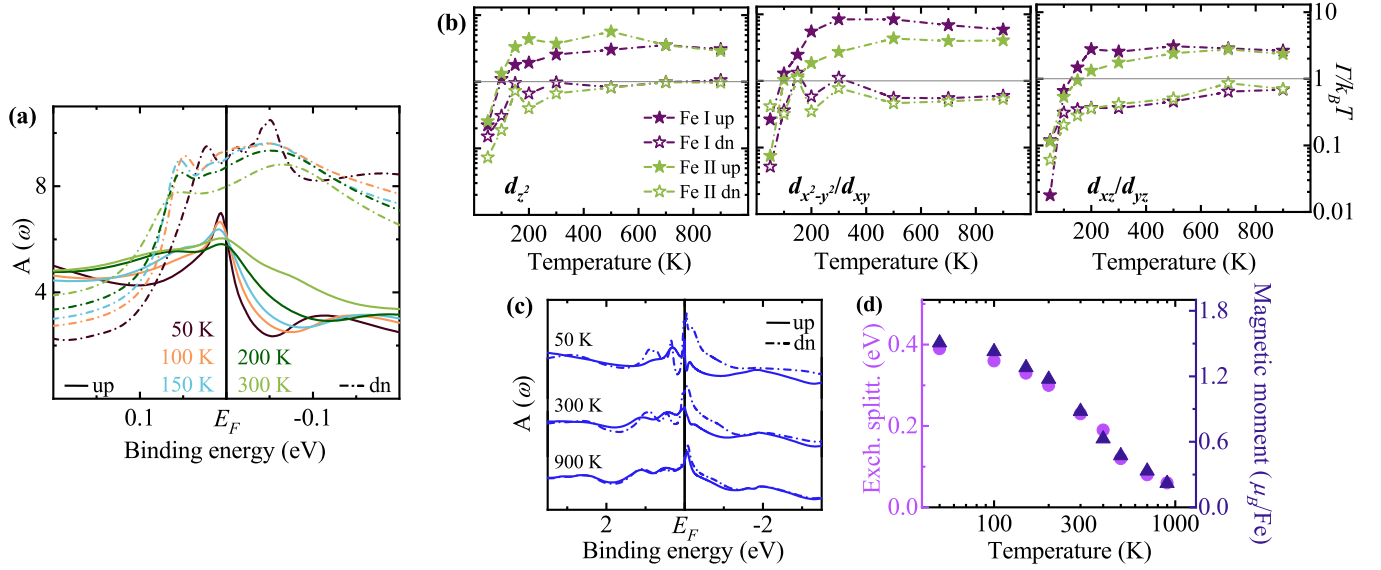
FIG. 4. Temperature-dependent FM DFT+DMFT results. (a) Spin-up (solid line) and spin-down (dash-dotted line) Fe $3d$ spectral functions. (b) $\Gamma/k_B T$ for the three nondegenerate orbitals (including both spins) for both Fe. Spin up (solid markers) and spin down (open markers) for Fe I (dark purple) and Fe II (green). (c) Spin-polarized total spectral functions and (d) exchange splitting (circles) and magnetic moments (triangles) at various temperatures.

calculations. The evolution of the quasiparticle peak with decreasing temperature is also well captured within the FM DFT+DMFT calculations; the spin-polarized Fe spectral functions are shown in Fig. 4(a). Intriguingly, we observe that the spin-down spectral functions remain largely unchanged around E_F; however, the spin-up spectral functions demonstrate the emergence of a quasiparticle peak just below E_F with decreasing temperature, implying significant influence of spin-differentiated electron correlation in Fe_3GeTe_2. Further, the scattering rate Γ was obtained for all the orbitals (including spin) for both Fe sites (see Appendix B), and $\Gamma/k_B T$ for various temperatures is shown in Fig. 4(b). These results unveil that Γ for spin-down channels for both Fe sites remain below $k_B T$, irrespective of temperature, suggesting the coherent scenario, while the spin-up channels show an incoherent-coherent crossover only below 150 K. It should be noted that the zero-frequency limit of the imaginary part of the self-energy on the imaginary frequency axis $Im\Sigma(i\omega \rightarrow 0^+)$ and thus the Γ approach zero faster with decreasing temperature for the spin-up channels than for the spin-down channels for all the orbitals of both Fe sites.

Within the itinerant electron magnetism, the exchange splitting of nondegenerate spin bands can be defined via various approaches [11,14,40,42,54]. In the DFT band scenario, the k-dependent exchange splitting can be estimated from the difference in the Kohn-Sham eigenvalues of spin split bands, and the k averaging gives a reasonable estimate [11]. However, a similar analysis cannot be performed using DFT+DMFT due to the diffusive and incoherent nature of the k-resolved spectral function [42]. Here, we attempt to estimate the exchange splitting in the Fe bands from the energy difference of the center of the weight of spin up and spin down from k-integrated spectral functions. The calculated spin-polarized total spectral functions are shown in Fig. 4(c) for different

temperatures. The spectral function at 50 K reveals large exchange splitting which decreases with increasing temperature where both spin-up and spin-down spectral functions take on a similar structure. Interestingly, the spin-dependent spectral functions remain nondegenerate even above T_C up to 900 K. The estimated exchange splitting and obtained magnetic moment also follow a similar trend and remain finite up to 900 K, as shown in Fig. 4(d).

To further elucidate the spin-differentiated dual nature, k-resolved spin-polarized spectral functions for different temperatures obtained from FM DFT+DMFT calculations are shown in Fig. 5. A large number of dispersive bands in both spin channels show finite exchange splitting and confirm the itinerant character, while the nondispersive bands in the vicinity of E_F in the case of the spin-down channel at high-temperature suggest a mixture of localized and itinerant electrons in Fe_3GeTe_2. Electronic structure calculations within the DFT+DMFT framework hugely overestimate the ferromagnetic transition and reveal no significant change in the valence band across T_C, hence providing additional evidence to conclude that Fe_3GeTe_2 is a non-Stoner ferromagnet in which the temporal and spatial thermal fluctuations lead to a disordered moment (itinerant and local both), thereby destroying the long-range magnetic order beyond T_C. The Stoner model provides a framework for itinerant magnetic materials; however, the inaccurate consideration of spin density fluctuation effects results in many limitations like overestimating T_C and Curie-Weiss behavior at higher temperatures [15,27]. Thus, these results encourage the use of spin-resolved (AR)PES to further understand the electronic structure of Fe_3GeTe_2 across T_C. In addition, diffusive bands in spin-up k-resolved spectral functions representing incoherent states show a crossover to sharp and coherent states with decreasing temperature, while spin-down channels remain very
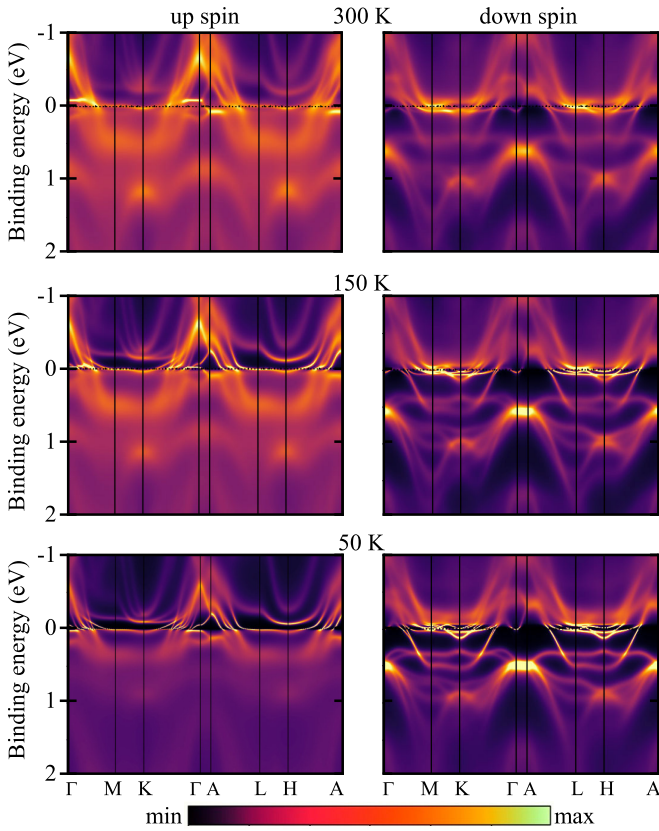
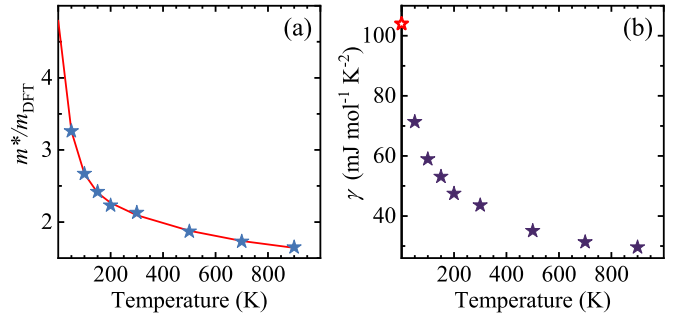FIG. 5. *k*-resolved spectral functions from FM DFT+DMFT for the spin up (left) and spin down (right) at 300, 150, and 50 K.

FIG. 6. Calculated (a) mass enhancement factor m^*/m_{DFT} and (b) Sommerfeld coefficient γ using FM DFT+DMFT calculations at various temperatures. The red line in (a) shows the fitting using the double-exponential function ($y_0 + a_1 e^{(-x/t_1)} + a_2 e^{(-x/t_2)}$), where $y_0 = 1.45$, $a_1 = 2.17$, $a_2 = 1.17$, $t_1 = 47.03$, and $t_2 = 498.22$), and the open star in (b) shows the calculated γ obtained using an extrapolated value of the mass enhancement factor at 0 K.

similar. The spectral function obtained from low-temperature DFT+DMFT is in reasonable agreement with experimental band dispersion along the M-Γ-K directions (shown in Appendix A). Further, observed dispersive energy bands along the Γ-A direction in k-resolved spectral functions at low temperatures imply significant interlayer coupling and thus three-dimensionality of the electronic structure in Fe$_3$GeTe$_2$ [14]. The lower Fermi velocity of spin split bands in Fe$_3$GeTe$_2$ than in the case of a typical metal along with hybridization of these flat bands with strongly dispersive bands near E_F suggests strengthened quasiparticle mass [13,24].

Finally, we discuss the discrepancy related to the mass enhancement factor m^*/m_e in the literature [13,14,25,26,43]. The Sommerfeld coefficient γ (110 mJ mol^{-1} K^{-2}) obtained from specific heat measurement is much larger than that of the free electron value of ≈ 6 mJ mol^{-1} K^{-2} considering six-electron occupancy per Fe, leading to the heavy-fermionic system with m^*/m_e of ≈ 18 [25,55]. As discussed earlier, the large reduction in DOS(E_F) obtained in the FM DFT results (with respect to the NM DFT results) is in strong disagreement with PES results and also leads to an overestimation of $\frac{m^*}{m_{DFT}} = 14.12$ (see Fig. S4 in the SM [28]). Within the DFT+DMFT framework, $\frac{m^*}{m_{DFT}}$ is the weighted sum of contributions arising from all the orbitals l and spins s, weighted by their local Green's function ($\propto$ partial DOS) at E_F [43,45]. $\frac{m^*}{m_{DFT}}$ obtained from FM DFT+DMFT calculations as shown in Fig. 6(a) reveals increasing mass enhancement with decreasing temperature, with $\frac{m^*}{m_{DFT}} = 3.26$ at 50 K, suggesting Fe$_3$GeTe$_2$ is

a heavy-fermionic system at low temperature. γ_{DMFT} obtained with a linear sum of each contribution $\gamma_{l,s}$ ($\gamma_{DMFT} = \sum_{l,s} \gamma_{l,s} = \sum_{l,s} [(\pi^2 k_B^2/3) \frac{m^*}{m_b}|_{l,s}$ PDOS$_{l,s}] \approx [(\pi^2 k_B^2/3) \frac{m^*}{m_{DFT}}$ A(ω)]) [45] leads to ~ 70 mJ mol^{-1} K^{-2} at 50 K. The extrapolated value of $\frac{m^*}{m_{DFT}}$ of 4.79 at 0 K leads to γ of ~ 104 mJ mol^{-1} K^{-2}, as shown in Fig. 6(b), which is in close agreement with experiments, finally resolving the much debated disparity [25].

IV. CONCLUSION

In summary, the electronic structure of Fe$_3$GeTe$_2$ was investigated using photoemission spectroscopy and theoretical calculations within the DFT, DFT+U, and DFT+DMFT frameworks. The high-resolution valence band spectra are well captured within DFT+DMFT across the magnetic phase transition. Temperature-dependent high-resolution spectra exhibit the emergence of a quasiparticle peak in close proximity to E_F along with the manifestation of an incoherent-coherent crossover in which anomalous behavior of the spectral density of states at E_F is observed at ~ 125 K. DFT+DMFT successfully demonstrated the evolution of spin bands with an incoherent-coherent crossover along increasing effective mass at lower temperatures, proving the heavy-fermionic nature. We also resolved the long-standing issue of the large Sommerfeld coefficient in this system obtained with DFT+DMFT calculations. In particular, (1) the lack of significant change in the experimental Fe 2p core level and overall valence band across T_C and (2) finite exchange splitting (also magnetic moment) persisting even beyond 4T_C in temperature-dependent ferromagnetic DFT+DMFT calculations together suggest Fe$_3$GeTe$_2$ is a non-Stoner ferromagnet. The results presented here advance the understanding of the complex evolution of the electronic structure and non-Stoner magnetic behavior and lay the foundation for further spin-resolved PES in the correlated van der Waals ferromagnet Fe$_3$GeTe$_2$.
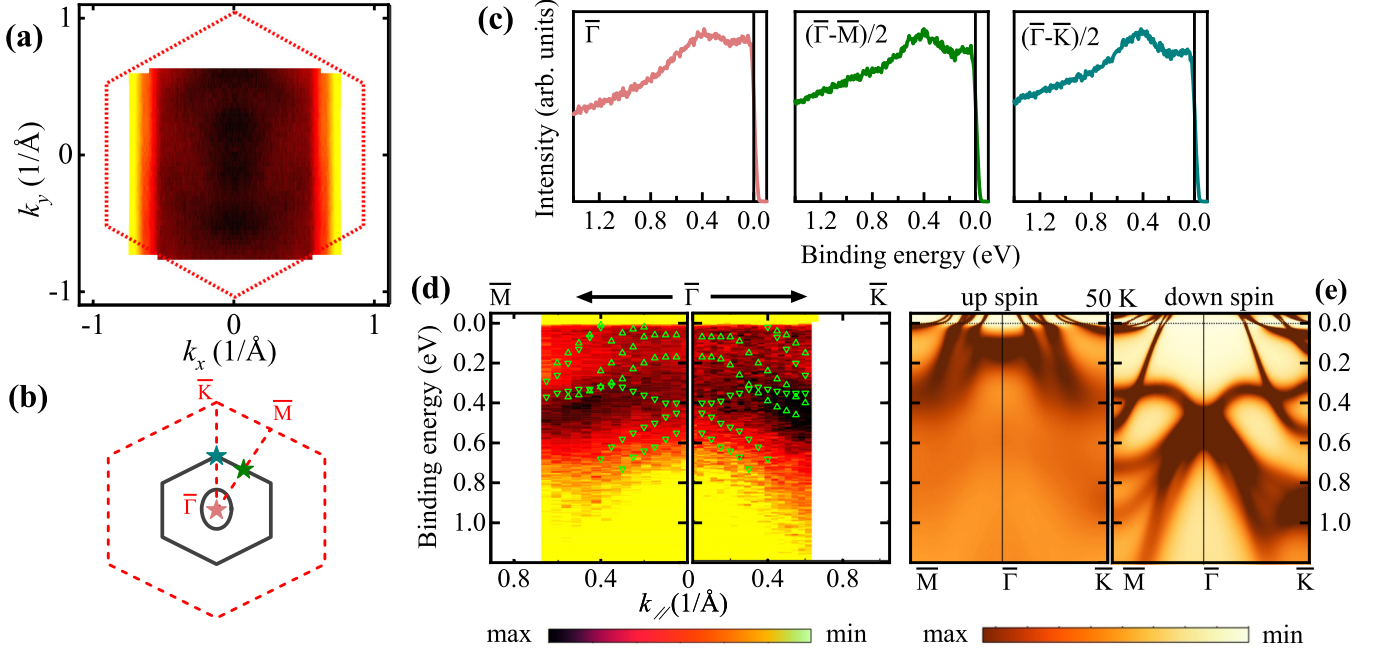
ACKNOWLEDGMENTS

FIG. 7. (a) Fermi surface map of Fe_3GeTe_2 using He I radiation at 30 K and (b) schematic diagram. The red dashed line shows the Brillouin zone with high-symmetry directions in (b). The stars marked in (b) in pink, green, and blue represent the $\overline{\Gamma}$, $(\overline{\Gamma}\text{-}\overline{M})/2$, and $(\overline{\Gamma}\text{-}\overline{K})/2$ locations, respectively, along which (c) energy distribution curves are shown. (d) ARPES band dispersion and (e) k-resolved spectral function at $k_z = 0.353c^*$ from FM DFT+DMFT ($T = 50$ K) for both the spin bands along the high-symmetry directions. For better visualization the high-intensity bands from up and down spins of the k-resolved spectral functions are overlapped on the ARPES band dispersion using up and down green triangles, respectively.

APPENDIX A: ARPES RESULTS AND ANALYSIS

The ARPES Fermi surface map (integrated within the $E_F \pm 10$ meV energy window and symmetrized along the $k_x = 0$ line) obtained using He I radiation ($k_z = 0.353c^*$, considering the inner potential $V_0 = 13.5$ eV [14]) at 30 K (with a total energy resolution $\sim$15 meV) is shown in Fig. 7(a). The circular and hexagonal Fermi surfaces centered around $\overline{\Gamma}$ are in agreement with earlier observations [13,14]. Figure 7(b) shows a schematic of the obtained Fermi surfaces, where the dashed red hexagon represents the surface Brillouin zone with high-symmetry lines $\overline{\Gamma}\text{-}\overline{K}$, and $\overline{\Gamma}\text{-}\overline{M}$. The stars represents $\overline{\Gamma}$, $(\overline{\Gamma}\text{-}\overline{M})/2$, and $(\overline{\Gamma}\text{-}\overline{K})/2$; the correspond energy distributive curves (EDCs; integrated for Δk_x and Δk_y within ± 0.02 Å^{-1}) are shown in Fig. 7(c). A strengthened quasiparticle peak ($\sim$40 meV BE) is evident from the EDC at $\overline{\Gamma}$, compared to the same obtained from the EDCs at $(\overline{\Gamma}\text{-}\overline{M})/2$ and $(\overline{\Gamma}\text{-}\overline{K})/2$. It should be noted that the overall EDCs at various locations across the Brillouin zone are mostly similar and agree well

with the momentum-integration high-resolution PES spectra presented in the main text [Fig. 3(a)]. Further, Figs. 7(d) and 7(e) represent the band dispersion from ARPES (at 30 K) and k-resolved spectral functions of both the spins from the FM DFT+DMFT calculation (at 50 K, $k_z = 0.353c^*$), respectively, along high-symmetry directions. ARPES spectra [Fig. 7(d)] show broad (incoherentlike) bands at around 0.4 eV BE and sharper (coherentlike) bands around E_F in $\overline{M}\text{-}\overline{\Gamma}$ as well as in the $\overline{\Gamma}\text{-}\overline{K}$ direction, which are better resolved in both spin channels of k-resolved spectral functions of DFT+DMFT. For better visualization, the bands with higher spectral functions from the DFT+DMFT results are overlapped on the ARPES spectra (using markers) in Fig. 7(d), with up and down green triangles for up spin and down spin, respectively.

APPENDIX B: DFT+DMFT RESULTS AND ANALYSIS

Within the FM DFT+DMFT calculation the spin- and orbital-dependent imaginary part of the self-energy on the Matsubara frequency axis $\text{Im}\Sigma(i\omega)$ for both Fe sites was obtained and is shown in Fig. 8(a) for $T = 50$ K. $\text{Im}\Sigma(i\omega)$ approaches zero at lower frequency for all the orbitals and spins of both Fe sites. The quasiparticle scattering rate is calculated using $\Gamma_{l,s} = -(m^*/m_b)_{l,s}^{-1} \text{Im}\Sigma_{l,s}(i\omega \to 0^+)$, where $(m^*/m_b)_{l,s} = 1 - \partial\text{Im}\Sigma_{l,s}(i\omega)/\partial(i\omega)|_{i\omega \to 0}$ for l orbitals and s spins, and is shown in Fig. 8(b) [43,45] for various temperatures. The imaginary part of the self-energy at the zero-frequency limit and its derivative were obtained using
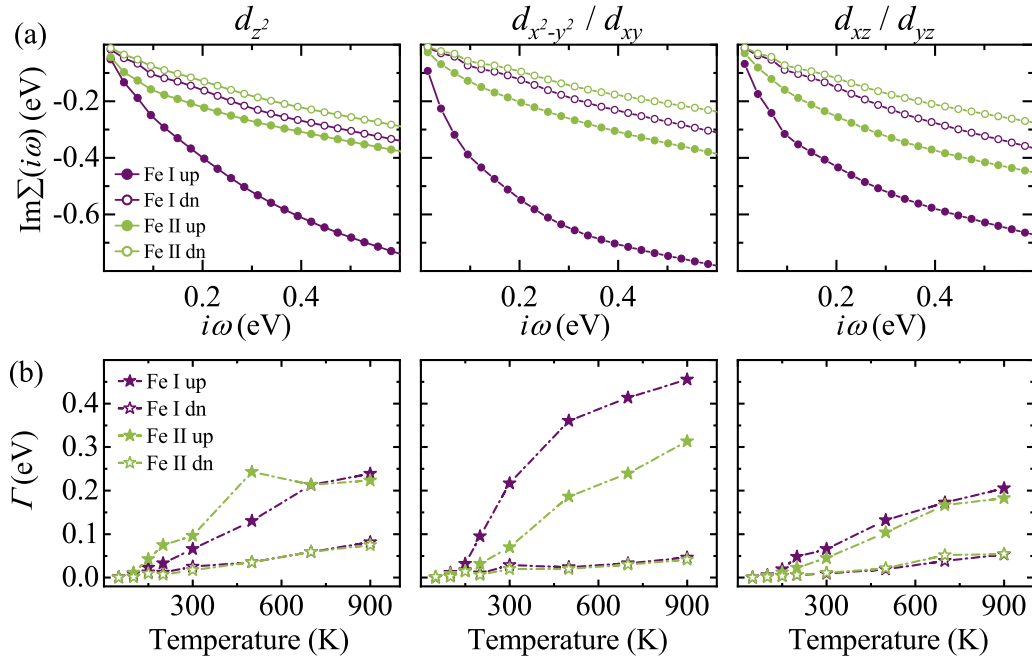
FIG. 8. (a) Spin- and orbital-dependent imaginary part of the self-energy on the Matsubara frequency axis $\mathrm{Im}\Sigma(i\omega)$ for both Fe sites using FM DFT+DMFT calculations at 50 K. (b) Quasiparticle scattering rate Γ for the three nondegenerate orbitals (including spin) for both Fe sites at various temperatures. Spin up and spin down are shown by solid markers and open markers, respectively, for Fe I (dark purple) and Fe II (green).

a fourth-order polynomial fit for the first six data points. The spin-up channels for both Fe sites exhibit larger $\mathrm{Im}\Sigma_l$ $(i\omega \to 0^+)$ for all the orbitals at higher temperature and tend to zero faster at lower temperature in comparison to the spin-down channels, implying a significant influence of the spin-differentiated electron correlation in Fe_3GeTe_2. The overall trend of $\Gamma_{l,s}$ is consistent with the imaginary part of the

self-energy at the zero-frequency limit. Further, Γ obtained for all the orbitals for both Fe sites reveals that the spin-down channels remain below $k_B T$ [as shown in Fig. 4(b)], irrespective of the temperature for both Fe sites, suggesting the coherent scenario throughout, while the spin-up channels show an incoherent-coherent crossover only below 150 K.

[1] K. F. Mak, J. Shan, and D. C. Ralph, Probing and controlling magnetic states in 2D layered magnetic materials, Nat. Rev. Phys. **1**, 646 (2019).

[2] M. Gibertini, M. Koperski, A. F. Morpurgo, and K. S. Novoselov, Magnetic 2D materials and heterostructures, Nat. Nanotechnol. **14**, 408 (2019).

[3] K. S. Burch, D. Mandrus, and J.-G. Park, Magnetism in two-dimensional van der Waals materials, Nature (London) **563**, 47 (2018).

[4] C. Gong, L. Li, Z. Li, H. Ji, A. Stern, Y. Xia, T. Cao, W. Bao, C. Wang, Y. Wang, Z. Q. Qiu, R. J. Cava, S. G. Louie, J. Xia, and X. Zhang, Discovery of intrinsic ferromagnetism in two-dimensional van der Waals crystals, Nature (London) **546**, 265 (2017).

[5] T. J. Williams, A. A. Aczel, M. D. Lumsden, S. E. Nagler, M. B. Stone, J.-Q. Yan, and D. Mandrus, Magnetic correlations in the quasi-two-dimensional semiconducting ferromagnet CrSiTe₃, Phys. Rev. B **92**, 144404 (2015).

[6] B. Huang, G. Clark, E. Navarro-Moratalla, D. R. Klein, R. Cheng, K. L. Seyler, D. Zhong, E. Schmidgall, M. A. McGuire, D. H. Cobden, W. Yao, D. Xiao, P. Jarillo-Herrero, and X. Xu, Layer-dependent ferromagnetism in a van der Waals crystal down to the monolayer limit, Nature (London) **546**, 270 (2017).

[7] Y. Deng, Y. Yu, Y. Song, J. Zhang, N. Z. Wang, Z. Sun, Y. Yi, Y. Z. Wu, S. Wu, J. Zhu, J. Wang, X. H. Chen, and Y. Zhang, Gate-tunable room-temperature ferromagnetism in two-dimensional Fe_3GeTe_2, Nature (London) **563**, 94 (2018).

[8] M. T. Birch, L. Powalla, S. Wintz, O. Hovorka, K. Litzius, J. C. Loudon, L. A. Turnbull, V. Nehruji, K. Son, C. Bubeck, T. G. Rauch, M. Weigand, E. Goering, M. Burghard, and G. Schütz, History-dependent domain and skyrmion formation in 2D van der Waals magnet Fe_3GeTe_2, Nat. Commun. **13**, 3035 (2022).

[9] R. R. Chowdhury, S. DuttaGupta, C. Patra, O. A. Tretiakov, S. Sharma, S. Fukami, H. Ohno, and R. P. Singh, Unconventional Hall effect and its variation with co-doping in van der Waals Fe_3GeTe_2, Sci. Rep. **11**, 14121 (2021).

[10] R. Roy Chowdhury, C. Patra, S. DuttaGupta, S. Satheesh, S. Dan, S. Fukami, and R. P. Singh, Modification of unconventional Hall effect with doping at the nonmagnetic site in a two-dimensional van der Waals ferromagnet, Phys. Rev. Mater. **6**, 014002 (2022).

[11] H. L. Zhuang, P. R. C. Kent, and R. G. Hennig, Strong anisotropy and magnetostriction in the two-dimensional Stoner ferromagnet Fe_3GeTe_2, Phys. Rev. B **93**, 134407 (2016).

[12] D. Yuan, S. Jin, N. Liu, S. Shen, Z. Lin, K. Li, and X. Chen, Tuning magnetic properties in quasi-two-dimensional

ferromagnetic $Fe_{3-y}Ge_{1-x}As_xTe_2$ ($0 \leqslant x \leqslant 0.85$), Mater. Res. Express **4**, 036103 (2017).

[13] Y. Zhang, H. Lu, X. Zhu, S. Tan, W. Feng, Q. Liu, W. Zhang, Q. Chen, Y. Liu, X. Luo, D. Xie, L. Luo, Z. Zhang, and X. Lai, Emergence of Kondo lattice behavior in a van der Waals itinerant ferromagnet, Fe_3GeTe_2, Sci. Adv. **4**, eaao6791 (2018).

[14] X. Xu, Y. W. Li, S. R. Duan, S. L. Zhang, Y. J. Chen, L. Kang, A. J. Liang, C. Chen, W. Xia, Y. Xu, P. Malinowski, X. D. Xu, J.-H. Chu, G. Li, Y. F. Guo, Z. K. Liu, L. X. Yang, and Y. L. Chen, Signature for non-Stoner ferromagnetism in the van der Waals ferromagnet Fe_3GeTe_2, Phys. Rev. B **101**, 201104(R) (2020).

[15] J. M. Santiago, C.-L. Huang, and E. Morosan, Itinerant magnetic metals, J. Phys.: Condens. Matter **29**, 373002 (2017).

[16] V. Korenman, J. L. Murray, and R. E. Prange, Local-band theory of itinerant ferromagnetism. I. Fermi-liquid theory, Phys. Rev. B **16**, 4032 (1977).

[17] K. Maiti, M. C. Malagoli, A. Dallmeyer, and C. Carbone, Finite temperature magnetism in Gd: Evidence against a Stoner behavior, Phys. Rev. Lett. **88**, 167205 (2002).

[18] D. C. Johnston, The puzzle of high temperature superconductivity in layered iron pnictides and chalcogenides, Adv. Phys. **59**, 803 (2010).

[19] P. Hansmann, R. Arita, A. Toschi, S. Sakai, G. Sangiovanni, and K. Held, Dichotomy between large local and small ordered magnetic moments in iron-based superconductors, Phys. Rev. Lett. **104**, 197002 (2010).

[20] P. Dai, J. Hu, and E. Dagotto, Magnetism and its microscopic origin in iron-based high-temperature superconductors, Nat. Phys. **8**, 709 (2012).

[21] K. Haule and G. Kotliar, Coherence-incoherence crossover in the normal state of iron oxypnictides and importance of Hund's rule coupling, New J. Phys. **11**, 025021 (2009).

[22] X. Bai, F. Lechermann, Y. Liu, Y. Cheng, A. I. Kolesnikov, F. Ye, T. J. Williams, S. Chi, T. Hong, G. E. Granroth, A. F. May, and S. Calder, Antiferromagnetic fluctuations and orbital-selective Mott transition in the van der Waals ferromagnet Fe_3GeTe_2, Phys. Rev. B **106**, L180409 (2022).

[23] M. Zhao, B.-B. Chen, Y. Xi, Y. Zhao, H. Xu, H. Zhang, N. Cheng, H. Feng, J. Zhuang, F. Pan, X. Xu, W. Hao, W. Li, S. Zhou, S. X. Dou, and Y. Du, Kondo holes in the two-dimensional itinerant Ising ferromagnet Fe_3GeTe_2, Nano Lett. **21**, 6117 (2021).

[24] D. Rana, A. R, B. G, C. Patra, S. Howlader, R. R. Chowdhury, M. Kabir, R. P. Singh, and G. Sheet, Spin-polarized supercurrent through the van der Waals Kondo-lattice ferromagnet Fe_3GeTe_2, Phys. Rev. B **106**, 085120 (2022).

[25] J.-X. Zhu, M. Janoschek, D. S. Chaves, J. C. Cezar, T. Durakiewicz, F. Ronning, Y. Sassa, M. Mansson, B. L. Scott, N. Wakeham, E. D. Bauer, and J. D. Thompson, Electronic correlation and magnetism in the ferromagnetic metal Fe_3GeTe_2, Phys. Rev. B **93**, 144404 (2016).

[26] K. Kim, J. Seo, E. Lee, K.-T. Ko, B. S. Kim, B. G. Jang, J. M. Ok, J. Lee, Y. J. Jo, W. Kang, J. H. Shim, C. Kim, H. W. Yeom, B. II Min, B.-J. Yang, and J. S. Kim, Large anomalous Hall current induced by topological nodal lines in a ferromagnetic van der Waals semimetal, Nat. Mater. **17**, 794 (2018).

[27] B. Chen, J. Yang, H. Wang, M. Imai, H. Ohta, C. Michioka, K. Yoshimura, and M. Fang, Magnetic properties of layered itinerant electron ferromagnet Fe_3GeTe_2, J. Phys. Soc. Jpn. **82**, 124711 (2013).

[28] See Supplemental Material at http://link.aps.org/supplemental/10.1103/PhysRevB.110.125119 for experimental details and analysis and for further DFT and DFT+DMFT results.

[29] P. Blaha, K. Schwarz, F. Tran, R. Laskowski, G. K. H. Madsen, and L. D. Marks, Wien2k: An APW+lo program for calculating the properties of solids, J. Chem. Phys. **152**, 074101 (2020).

[30] J. P. Perdew, K. Burke, and M. Ernzerhof, Generalized gradient approximation made simple, Phys. Rev. Lett. **77**, 3865 (1996).

[31] K. Haule, C.-H. Yee, and K. Kim, Dynamical mean-field theory within the full-potential methods: Electronic structure of $CeIrIn_5$, $CeCoIn_5$, and $CeRhIn_5$, Phys. Rev. B **81**, 195107 (2010).

[32] K. Haule, Quantum Monte Carlo impurity solver for cluster dynamical mean-field theory and electronic structure calculations with adjustable cluster base, Phys. Rev. B **75**, 155113 (2007).

[33] K. Haule, Exact double counting in combining the dynamical mean field theory and the density functional theory, Phys. Rev. Lett. **115**, 196403 (2015).

[34] G. Rossi, G. Panaccione, F. Sirotti, S. Lizzit, A. Baraldi, and G. Paolucci, Magnetic dichroism in the angular distribution of Fe 2p and 3p photoelectrons: Empirical support to Zeeman-like analysis, Phys. Rev. B **55**, 11488 (1997).

[35] J. F. Moulder, W. F. Stickle, P. E. Sobol, and K. D. Bomben, *Handbook of X-ray Photoelectron Spectroscopy* (Perkin-Elmer Corporation, Eden Prairie, MN, 1992).

[36] S. Sarkar, P. Sadhukhan, V. K. Singh, A. Gloskovskii, K. Deguchi, N. Fujita, and S. R. Barman, Bulk electronic structure of high-order quaternary approximants, Phys. Rev. Res. **3**, 013151 (2021).

[37] L. Baumgarten, C. M. Schneider, H. Petersen, F. Schäfers, and J. Kirschner, Magnetic x-ray dichroism in core-level photoemission from ferromagnets, Phys. Rev. Lett. **65**, 492 (1990).

[38] J. G. Menchero, One-electron theory of core-level photoemission from ferromagnets, Phys. Rev. B **57**, 993 (1998).

[39] J. J. Yeh and I. Lindau, Atomic subshell photoionization cross sections and asymmetry parameters: $1 \leqslant Z \leqslant 103$, At. Data Nucl. Data Tables **32**, 1 (1985).

[40] M. Kim and B. I. Min, Nature of itinerant ferromagnetism of $SrRuO_3$: A DFT+DMFT study, Phys. Rev. B **91**, 205116 (2015).

[41] R. S. Singh, V. R. R. Medicherla, and K. Maiti, Role of long range ferromagnetic order in the electronic structure of $Sr_{1-x}Ca_xRuO_3$, Appl. Phys. Lett. **91**, 132503 (2007).

[42] S. Ghosh, S. Ershadrad, V. Borisov, and B. Sanyal, Unraveling effects of electron correlation in two-dimensional Fe_nGeTe_2 (n = 3, 4, 5) by dynamical mean field theory, npj Comput. Mater. **9**, 86 (2023).

[43] T. J. Kim, S. Ryee, and M. J. Han, Fe_3GeTe_2: A site-differentiated Hund metal, npj Comput. Mater. **8**, 245 (2022).

[44] A. Paul and T. Birol, Applications of DFT + DMFT in materials science, Annu. Rev. Mater. Res. **49**, 31 (2019).

[45] G. Kotliar, S. Y. Savrasov, K. Haule, V. S. Oudovenko, O. Parcollet, and C. A. Marianetti, Electronic structure calculations with dynamical mean-field theory, Rev. Mod. Phys. **78**, 865 (2006).

[46] Z. Zhou, S. K. Pandey, and J. Feng, Dynamical correlation enhanced orbital magnetization in VI_3, Phys. Rev. B **103**, 035137 (2021).

[47] Y. O. Kvashnin, A. N. Rudenko, P. Thunström, M. Rösner, and M. I. Katsnelson, Dynamical correlations in single-layer CrI_3, Phys. Rev. B **105**, 205124 (2022).

[48] K. Maiti, A. Kumar, D. D. Sarma, E. Weschke, and G. Kaindl, Surface and bulk electronic structure of $La_{1−x}Ca_xVO_3$, Phys. Rev. B **70**, 195112 (2004); K. Maiti, R. S. Singh, V. R. R. Medicherla, S. Rayaprol, and E. V. Sampathkumaran, Origin of charge density wave formation in insulators from a high resolution photoemission study of $BaIrO_3$, Phys. Rev. Lett. **95**, 016404 (2005); S. Bansal, R. K. Maurya, A. Ali, B. H. Reddy, and R. S. Singh, Role of electron correlation and disorder on the electronic structure of layered nickelate $(La_{0.5}Sr_{0.5})_2NiO_4$, Phys. Rev. Mater. **7**, 064007 (2023).

[49] M. R. Norman, H. Ding, M. Randeria, J. C. Campuzano, T. Yokoya, T. Takeuchi, T. Takahashi, T. Mochiku, K. Kadowaki, P. Guptasarma, and D. G. Hinks, Destruction of the Fermi surface in underdoped high-Tc superconductors, Nature (London) **392**, 157 (1998); R. S. Singh, V. R. R. Medicherla, K. Maiti, and E. V. Sampathkumaran, Evidence for strong 5d electron correlations in the pyrochlore $Y_2Ir_2O_7$ studied using high-resolution photoemission spectroscopy, Phys. Rev. B **77**, 201102(R) (2008); B. H. Reddy, A. Ali, and R. S. Singh,

Role of disorder and strong 5d electron correlation in the electronic structure of Sr_2TiIrO_6, Europhys. Lett. **127**, 47003 (2019).

[50] H. Hegger, C. Petrovic, E. G. Moshopoulou, M. F. Hundley, J. L. Sarrao, Z. Fisk, and J. D. Thompson, Pressure-induced superconductivity in quasi-2D $CeRhIn_5$, Phys. Rev. Lett. **84**, 4986 (2000).

[51] C. Krellner, T. Förster, H. Jeevan, C. Geibel, and J. Sichelschmidt, Relevance of ferromagnetic correlations for the electron spin resonance in Kondo lattice systems, Phys. Rev. Lett. **100**, 066401 (2008).

[52] Z. Fisk, D. W. Hess, C. J. Pethick, D. Pines, J. L. Smith, J. D. Thompson, and J. O. Willis, Heavy-electron metals: New highly correlated states of matter, Science **239**, 33 (1988).

[53] J. Mravlje, M. Aichhorn, T. Miyake, K. Haule, G. Kotliar, and A. Georges, Coherence-incoherence crossover and the mass-renormalization puzzles in Sr_2RuO_4, Phys. Rev. Lett. **106**, 096401 (2011).

[54] Y. O. Kvashnin, O. Grånäs, I. Di Marco, M. I. Katsnelson, A. I. Lichtenstein, and O. Eriksson, Exchange parameters of strongly correlated materials: Extraction from spin-polarized density functional theory plus dynamical mean-field theory, Phys. Rev. B **91**, 125133 (2015).

[55] U. Mizutani, *Introduction to the Electron Theory of Metals* (Cambridge University Press, Cambridge, 2001).